A THEORETICAL ANALYSIS FOR PERISTALSIS OF CASSON MATERIAL WITH THERMAL RADIATION AND VISCOUS DISSIPATION

by

Shahid FAROOQ[a*], Tasawar HAYAT[a,b], and Bashir AHMAD[b]

[a] Department of Mathematics, Quaid-I-Azam University, Islamabad, Pakistan
[b] Nonlinear Analysis and Applied Mathematics (NAAM) Research Group,
Department of Mathematics, Faculty of Science,
King Abdulaziz University, Jeddah, Saudi Arabia

Original scientific paper
https://doi.org/10.2298/TSCI180104141F

Effects of thermal radiation and radial applied magnetic field on the peristaltic motion of Casson material in a channel are investigated. Heat equation contains Joule heating and viscous dissipation characteristics. The flow equations in wave frame are reduced in view of long wavelength and small Reynolds number. Stream function formulation is adopted. Closed form solutions of physical quantities have been developed. Physical interpretation through graphs is assigned. It is found that pressure gradient and fluid velocity decreases for Casson fluid parameter. Also temperature is decreasing quantity of thermal radiation parameter and Prandtl number.

Key words: *radial magnetic field, thermal radiation, Joule heating, Casson fluid*

Introduction

There is no doubt that peristaltic transport of fluid has relevance for chyme movement in the gastrointestinal tract, urine passage from kidney to bladder, blood circulation, locomotion of worms, ovum movement in the fallopian tube and spermatozoa in ductus efferents. Industrial applications of peristalsis may include transport of sanitary, corrosive and noxious materials. Roller and finger pumps and heart lung machine operate subject to principle of peristalsis. Such activity is also quite important in processes of pharmaceutical, cosmetic and paper industries. Having all such significance in mind, Latham [1] and Shapiro *et al.* [2] made earliest investigations for peristaltic transport of viscous fluid in a channel. Afterwards the peristaltic activity for viscous and non-Newtonian fluids has been analysed widely. Relevant information on the topic in view of diverse aspects is extensive. However few most recent attempts in this regard can be consulted via the refs. [3-12].

It is noted from the available information about peristalsis that mostly attention in the past has been focused to the flow in straight channels/uniform applied magnetic field. Consideration of magnetic field is important since many materials like corrosive, toxic, saline water and blood is electrically conducting. Further configuration in physiological and pipe flows are curved. With this view point some advancement is made to examine peristaltic flow of fluid in absence/presence of constant applied magnetic field. Mention may be made to the refs. [13-20] in this regard.

* Corresponding author, e-mail: sfarooq@math.qau.edu.pk

Moreover to achieve high targets, the thermal radiation depends on various types of physical systems like gas flow, heat, and mass transportation. Especially at high temperatures, the thermal radiation characteristics in heat transfer processes become provocatively more appreciable. Its acceptable applications in engineering are to design the diverse tools for satellites, aircrafts and different other space machines. Processes in which involves high temperature *e. g.* nuclear power plants, polymer and glass productions, gas turbines and so forth radiation mode contributes significantly. Impact of radiative convection in MHD flow of nanoliquid produced via non-linear boundary is explored by Pal and Mandal [21]. A numerical investigation for radiative MHD flow of Al_2O_3-water nanoparticles is delivered by Sheikholeslami *et al.* [22]. Hayat *et al.* [23, 24] addressed the thermally radiative stretchable flow of convected Eyring Powell and Maxwell liquids. Thermal radiation and magnetic field impacts on 2-D Williamson nanofluid flow are reported by Bhatti and Rashidi [25]. Moreover few recent studies which comprise the thermal radiation aspects can be view through refrs. [26-30].

Viscoplastic liquids have a complex transformation between a liquid-like and a solid-like reaction. Such fluids can be characterized via yield stress. In such kind of material when ratio of the shear stress to the yield stress is less than the unity it behaves like solid and it deforms when this ratio is higher than unity. It shows shear-thinning characteristics for larger yield stress. Mostly the Casson [31], Herschel-Bulkley [32] and inelastic Bingham [33] models are considered to highlight the properties of viscoplastic materials. In these three fluid models the most simplest model is Bingham liquid model, this model deals only with a yield stress. Due to its simplicity, the most frequently considered model in numerical and theoretical investigation is the Bingham fluid model. But this model is not realistic for all rheological materials. Because mostly the real fluids characterized as shear-thinning yield stress materials like Herschel-Bulkley/Casson liquids. Currently the Casson model is used in food stuff processing's [34]. Also this model has been utilized to model the rheological behavior of chocolate by the International Office of Cocoa and Chocolate. Furthermore, various working materials *e. g.* molten plastics, artificial fibers, polymeric materials, foodstuffs, blood, slurries and synovial liquids which demonstrate characteristics non-Newtonian liquids. Liquids of such kinds having relationships in the form of shear-stress-strain which are materially dissimilar from the viscous model. Various non-Newtonian models require some form of amendment to the momentum constraints. In the category of these non-Newtonian materials, the Casson material has different key features. In polymer processing industry and in the field of biomechanics it has considerable demands. Sometimes the Casson material is found very better for rheological data when compared with general viscoplastic models for various fluids. In the above aforementioned context, various researchers, [35-45] and several references therein are studied the heat transfer flow of Casson liquid with distinct physical aspects.

The purpose of present communication is to address the peristaltic flow of Casson material in a curved channel. Flow formulation is constructed in presence of radial applied magnetic field. Stream function formulation is followed. Large wavelength and low Reynolds number are taken into consideration for the whole computational analysis. Results for small occlusion are presented. The pressure gradient, pressure rise per wavelength, velocity, temperature and streamlines are analysed for the influences of Hartmann number, curvature, Casson parameter, amplitude ratio, Brinkman number, thermal radiation and Prandtl number.

Formulation

In fig. 1 we consider an incompressible fluid in a curved channel of width $2a_0$ coiled in a circle of radius R^* with centre lying at point O. Here $\bar{V}_1$ and $\bar{V}_2$ are the velocity components in radial ($\bar{R}$) and axial ($\bar{X}$) directions, respectively. Applied non-uniform magnetic field, B, is in the radial direction.

The fluid-flow inside the channel is due to peristaltic waves along the flexible wall of channel. Mathematical description of wall surfaces is:

$$\bar{H}\left(\bar{X},\bar{t}\right)=\pm\left\{a_0+a_1\sin\left[\frac{2\pi}{\lambda}\left(\bar{X}-c\bar{t}\right)\right]\right\} \tag{1}$$

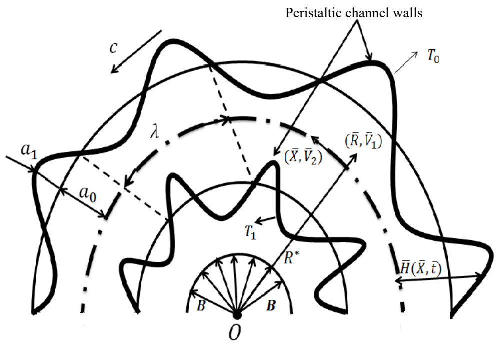

Figure 1. Physical diagram

In previous expression c denotes the wave speed, a_1 – the wave amplitude, λ – the wavelength, and $\bar{t}$ – the time in laboratory frame. The velocity, $\bar{\mathbf{V}}$, and extra stress tensor, $\bar{\mathbf{S}}$, for Casson fluid model are given:

$$\bar{\mathbf{V}}=[\bar{V}_1(\bar{X},\bar{R},\bar{t}),\bar{V}_2(\bar{X},\bar{R},\bar{t}),0] \tag{2}$$

$$\bar{\mathbf{S}}^{\frac{1}{n}}=\bar{\mathbf{S}}_0^{\frac{1}{n}}+\mu\ddot{\gamma}^{\frac{1}{n}} \tag{3}$$

$$\bar{\mathbf{S}}=\left(\mu_\beta+\frac{p_y}{\sqrt{2\pi_c}}\right)\bar{\mathbf{A}}_1 \tag{4}$$

where

$$\bar{\mathbf{A}}_1=\operatorname{grad}\bar{\mathbf{V}}+\left(\operatorname{grad}\bar{\mathbf{V}}\right)^* \tag{5}$$

The laws of conservation of mass, momentum and energy for the considered geometry are mentioned below [15-20]:

$$\frac{\partial}{\partial\bar{R}}\left[\left(R^*+\bar{R}\right)\bar{V}_1\right]+R^*\frac{\partial\bar{V}_2}{\partial\bar{X}}=0 \tag{6}$$

$$\rho\left[\frac{\partial\bar{V}_1}{\partial\bar{t}}+\bar{V}_1\frac{\partial\bar{V}_1}{\partial\bar{R}}+\frac{R^*\bar{V}_2}{R^*+\bar{R}}\frac{\partial\bar{V}_1}{\partial\bar{X}}-\frac{\bar{V}_2^2}{R^*+\bar{R}}\right]=-\frac{\partial\bar{p}}{\partial\bar{R}}+$$

$$+\frac{1}{R^*+\bar{R}}\frac{\partial}{\partial\bar{R}}\left[\left(R^*+\bar{R}\right)\bar{S}_{\bar{R}\bar{R}}\right]+\left(\frac{R^*}{R^*+\bar{R}}\right)\frac{\partial\bar{S}_{\bar{R}\bar{X}}}{\partial\bar{X}}-\frac{\bar{S}_{\bar{X}\bar{X}}}{R^*+\bar{R}} \tag{7}$$

$$\rho\left(\frac{\partial\bar{V}_2}{\partial\bar{t}}+\bar{V}_1\frac{\partial\bar{V}_2}{\partial\bar{R}}+\frac{R^*\bar{V}_2}{R^*+\bar{R}}\frac{\partial\bar{V}}{\partial\bar{X}}-\frac{\bar{V}_1\bar{V}_2}{R^*+\bar{R}}\right)=-\left(\frac{R^*}{R^*+\bar{R}}\right)\frac{\partial\bar{p}}{\partial\bar{X}}+$$

$$+\frac{1}{\left(R^*+\bar{R}\right)^2}\frac{\partial}{\partial\bar{R}}\left[\left(R^*+\bar{R}\right)^2\bar{S}_{\bar{R}\bar{X}}\right]+\left(\frac{R^*}{R^*+\bar{R}}\right)\frac{\partial\bar{S}_{\bar{X}\bar{X}}}{\partial\bar{X}}-\left(\frac{R'}{R'+\bar{R}}\right)^2\sigma B_0^2\bar{V}_2 \tag{8}$$

$$\rho c_p\left(\frac{\partial T}{\partial\bar{t}}+\bar{V}_1\frac{\partial T}{\partial\bar{R}}+\frac{\bar{V}_2R^*}{R^*+\bar{R}}\frac{\partial T}{\partial\bar{X}}\right)=\kappa\left[\frac{\partial^2T}{\partial\bar{R}^2}+\frac{1}{R^*+\bar{R}}\frac{\partial T}{\partial\bar{R}}+\frac{R^{*2}}{\left(R^*+\bar{R}\right)^2}\frac{\partial^2T}{\partial\bar{X}^2}\right]+$$

$$+\left(\frac{\partial \overline{V}_2}{\partial \overline{R}}-\frac{\overline{V}_2}{R^*+\overline{R}}+\frac{R^*}{R^*+\overline{R}}\frac{\partial \overline{V}_1}{\partial \overline{X}}\right)S_{\overline{R}\overline{X}}+\frac{\partial \overline{V}_2}{\partial \overline{R}}\left(S_{\overline{R}\overline{R}}-S_{\overline{X}\overline{X}}\right)+\left(\frac{R'}{R'+\overline{R}}\right)^2\sigma B_0^2\overline{V}_2^2-$$
$$-\frac{1}{R^*+\overline{R}}\frac{\partial}{\partial \overline{R}}\left[\left(R^*+\overline{R}\right)Q_{\overline{R}}\right] \tag{9}$$

In previous equations $\overline{P}$ denotes the pressure, ρ – the fluid density, $\overline{t}$ – the time, and $\overline{S}_{\overline{X}\overline{X}}$, $\overline{S}_{\overline{R}\overline{R}}$, $\overline{S}_{\overline{R}\overline{X}}$ – the extra stress components. Rossland approximation for thermal radiative flux is expressed [25-28]:

$$Q_{\overline{R}}=-\frac{16\sigma^* T_0^3}{3k^*}\frac{\partial T}{\partial \overline{R}} \tag{10}$$

in which σ^* the Stefan-Boltzmann and k^* – the mean absorption quantities, respectively. Note that flow is unsteady in fixed frame $(\overline{R},\overline{X})$ whereas the flow in the channel can be treated as steady in wave frame $(\overline{r},\overline{x})$ moving with wave speed c. Relations between co-ordinates, velocity components and pressure in both frames are:

$$\overline{x}=\overline{X}-c\overline{t},\quad \overline{r}=\overline{R},\quad \overline{v}_1(\overline{x},\overline{r})=\overline{V}_1(\overline{X},\overline{R},\overline{t}),\quad \overline{v}_2(\overline{x},\overline{r})=\overline{V}_2(\overline{X},\overline{R},\overline{t})-c$$
$$\overline{p}(\overline{x},\overline{r})=\overline{P}(\overline{X},\overline{R},\overline{t}),\ T(\overline{x},\overline{r})=T(\overline{X},\overline{R},\overline{t}) \tag{11}$$

where ($\overline{x}$, $\overline{r}$), ($\overline{v}_1$, $\overline{v}_2$), and $\overline{p}$ are, respectively, the co-ordinates, velocity components and pressure in wave frame. Now eqs. (6)-(9) yields:

$$\frac{\partial}{\partial \overline{r}}\left[\left(R^*+\overline{r}\right)\overline{v}_1\right]+R^*\frac{\partial \overline{v}_2}{\partial \overline{x}}=0 \tag{12}$$

$$\rho\left[-c\frac{\partial \overline{v}_1}{\partial \overline{x}}+\overline{v}_1\frac{\partial \overline{v}_1}{\partial \overline{r}}+\frac{R^*\left(\overline{v}_2+c\right)}{R^*+\overline{r}}\frac{\partial \overline{v}_1}{\partial \overline{x}}-\frac{\left(\overline{v}_2+c\right)^2}{R^*+\overline{r}}\right]=-\frac{\partial \overline{p}}{\partial \overline{r}}+$$
$$+\frac{1}{R^*+\overline{r}}\frac{\partial}{\partial \overline{r}}\left[\left(R^*+\overline{r}\right)\overline{S}_{\overline{r}\overline{r}}\right]+\left(\frac{R^*}{R^*+\overline{r}}\right)\frac{\partial \overline{S}_{\overline{r}\overline{x}}}{\partial \overline{x}}-\frac{\overline{S}_{\overline{x}\overline{x}}}{R^*+\overline{r}} \tag{13}$$

$$\rho\left[-c\frac{\partial \overline{v}_2}{\partial \overline{x}}+\overline{v}_1\frac{\partial \overline{v}_2}{\partial \overline{r}}+\frac{R^*\left(\overline{v}_2+c\right)}{R^*+\overline{r}}\frac{\partial \overline{v}_2}{\partial \overline{x}}-\frac{\overline{v}_1\overline{v}_2}{R^*+\overline{r}}\right]=-\left(\frac{R^*}{R^*+\overline{r}}\right)\frac{\partial \overline{p}}{\partial \overline{x}}+$$
$$+\frac{1}{\left(R^*+\overline{r}\right)^2}\frac{\partial}{\partial \overline{r}}\left[\left(R^*+\overline{r}\right)^2\overline{S}_{\overline{r}\overline{x}}\right]+\left(\frac{R^*}{R^*+\overline{r}}\right)\frac{\partial \overline{S}_{\overline{x}\overline{x}}}{\partial \overline{x}}-\left(\frac{R^*}{R^*+\overline{r}}\right)^2\sigma B_0^2\left(\overline{v}_2+c\right) \tag{14}$$

$$\rho c_p\left[-c\frac{\partial T}{\partial \overline{x}}+\overline{v}_1\frac{\partial T}{\partial \overline{r}}+\frac{\overline{V}_2 R^*}{R^*+\overline{r}}\frac{\partial T}{\partial \overline{x}}\right]=\kappa\left[\frac{\partial^2 T}{\partial \overline{r}^2}+\frac{1}{R^*+\overline{r}}\frac{\partial T}{\partial \overline{r}}+\frac{R^{*2}}{\left(R^*+\overline{r}\right)^2}\frac{\partial^2 T}{\partial \overline{x}^2}\right]+$$
$$+\left[\frac{\partial \overline{v}_2}{\partial \overline{r}}-\frac{\left(\overline{v}_2+c\right)}{R^*+\overline{r}}+\frac{R^*}{R^*+\overline{r}}\frac{\partial \overline{v}_1}{\partial \overline{x}}\right]S_{\overline{r}\overline{x}}+\frac{\partial \overline{v}_2}{\partial \overline{r}}\left(S_{\overline{r}\overline{r}}-S_{\overline{x}\overline{x}}\right)+\left(\frac{R^*}{R^*+\overline{r}}\right)^2\sigma B_0^2\left(\overline{v}_2+c\right)^2-$$
$$-\frac{1}{R^*+\overline{r}}\frac{\partial}{\partial \overline{r}}\left[\left(R^*+\overline{r}\right)Q_{\overline{r}}\right] \tag{15}$$

We further write the following dimensionless parameters:

$$x=\frac{2\pi\bar{x}}{\lambda_c},\quad t=\frac{c\bar{t}}{\lambda_c},\quad r=\frac{\bar{r}}{a_0},\quad v_1=\frac{\bar{v}_1}{c},\quad v_2=\frac{\bar{v}_2}{c},\quad \delta=\frac{2\pi a_0}{\lambda_c},\quad \eta=\pm\frac{\bar{H}}{a_0}$$

$$p=\frac{2\pi a_0^2\bar{p}}{c\mu_B\lambda_c},\quad k=\frac{R^*}{a_0},\quad \mathrm{M}=\left(\frac{\sigma}{\mu_B}\right)^{1/2}B_0a_0,\quad \mathrm{Re}=\frac{\rho c a_0}{\mu_B},\quad \mathrm{Pr}=\frac{\mu_0 c_p}{\kappa} \tag{16}$$

$$\theta=\frac{T-T_0}{T_1-T_0},\quad \mathrm{Ec}=\frac{c^2}{(T_1-T_0)c_p},\quad \mathrm{Br}=\mathrm{Pr}\,\mathrm{Ec},\quad R_d=\frac{16\sigma^*T_0^3}{3k^*\mu_B c_p},\quad S_{ij}=\frac{a_0}{c\mu_B}\bar{S}_{\bar{\bar{y}}}$$

where δ is the wave number, k – the curvature parameter, M – the Hartmann number, Re – the Reynolds number, Pr – the Prandtl number, Ec – the Eckert number, Br – the Brinkman number, and R_d – the thermal radiation constant.

The velocity components in terms of stream functions ψ can be defined:

$$v_1=\delta\frac{k}{r+k}\frac{\partial\psi}{\partial x},\quad v_2=-\frac{\partial\psi}{\partial r} \tag{17}$$

Physically it is found that large wavelength and small Reynolds are very useful for flow of chyme transportation in small intestine [46]. In small intestine wave speed $c = 2$ cm/min, width $a_0 = 1.25$ cm and wavelength $\lambda = 8.01$ cm. Also it is important to note that the half width of intestine is small in comparison to wavelength *i. e.* $a_0/\lambda = 0.156$. Lew *et al.* [47] also justified in their study that Reynolds number is very small in small intestine. Further several researchers use such assumption during studying peristalsis [48-50]. In view of all the mentioned facts eq. (12) is satisfied identically and assumptions of long wavelength and low Reynolds number further reduce the governing equations:

$$\frac{\partial p}{\partial r}=0 \tag{18}$$

$$\frac{k}{r+k}\frac{\partial p}{\partial x}=\frac{1}{(r+k)^2}\frac{\partial}{\partial r}\left[(r+k)^2S_{rx}\right]-\left(\frac{r\mathrm{M}}{r+k}\right)^2\left(1-\frac{\partial\psi}{\partial r}\right) \tag{19}$$

$$\left(1+\mathrm{Pr}\,R_d\right)\left(\frac{\partial^2\theta}{\partial r^2}+\frac{1}{r+k}\frac{\partial\theta}{\partial r}\right)+\mathrm{Br}\left(-\frac{\partial^2\psi}{\partial r^2}-\frac{1-\frac{\partial\psi}{\partial r}}{r+k}\right)S_{rx}+\mathrm{Br}\left(\frac{r\mathrm{M}}{r+k}\right)^2\left(1-\frac{\partial\psi}{\partial r}\right)^2=0 \tag{20}$$

with

$$S_{rx}=\left(1+\frac{1}{\xi}\right)\left(-\frac{\partial^2\psi}{\partial r^2}-\frac{1-\frac{\partial\psi}{\partial r}}{r+k}\right) \tag{21}$$

Dimensionless boundary conditions subject to the problem are:

$$\psi(r)=-\frac{F}{2},\quad \frac{\partial\psi}{\partial r}=1,\quad \theta=0\quad \text{at}\ r=+\eta \tag{22}$$

$$\psi(r)=\frac{F}{2},\quad \frac{\partial\psi}{\partial r}=1,\quad \theta=1\quad \text{at}\ r=-\eta \tag{23}$$

$$\eta(x)=\left[1+\epsilon\sin\left(2\pi x\right)\right] \tag{24}$$

where $\epsilon = a_1/a_0$ is the amplitude ratio or occlusion. Present study can be reduced to straight/planner channel when $k\to\infty$ (*i. e.* larger curvature parameter).

Solution methodology

Closed form solution for pressure gradient $\mathrm{d}p/\mathrm{d}x$, stream function, ψ, velocity, v_2 and temperature, θ, is of the form:

$$\psi\left(x,r\right)=C_3-\frac{1}{\mathrm{M}^2}\left[-r(2\mathrm{M}^2+k\frac{\mathrm{d}p}{\mathrm{d}x}(2k+r)\right]+2(k+r)\sqrt{1+\frac{1}{\xi}}\cdot$$

$$\cdot\left\{\left(\left(\sqrt{1+\frac{1}{\xi}}C_1-L_1C_2\right)\cos\left[\frac{L_2\log(k+r)}{\sqrt{1+\frac{1}{\xi}}}\right]+\left(L_1C_1+\sqrt{1+\frac{1}{\xi}}C_2\right)\sin\left[\frac{L_1\log(k+r)}{\sqrt{1+\frac{1}{\xi}}}\right]\right]\right\}$$

$$v_2\left(x,r\right)=-\frac{1}{\mathrm{M}^2}\left\{-\left[2\mathrm{M}^2+2k\frac{\mathrm{d}p}{\mathrm{d}x}(k+r)\right]+2L_1\left(L_1C_1+\sqrt{1+\frac{1}{\xi}}C_2\right)\cos\left[\frac{L_1\log(k+r)}{\sqrt{1+\frac{1}{\xi}}}\right]+\right.$$

$$+2\left(-L_1C_2+\sqrt{1+\frac{1}{\xi}}C_1\right)\sqrt{1+\frac{1}{\xi}}\cos\left[\frac{L_1\log(k+r)}{\sqrt{1+\frac{1}{\xi}}}\right]+$$

$$+2L_2\left(-L_1C_2+\sqrt{1+\frac{1}{\xi}}C_1\right)\sin\left[\frac{L_1\log(k+r)}{\sqrt{1+\frac{1}{\xi}}}\right]+$$

$$\left.+2\left(L_1C_1+\sqrt{1+\frac{1}{\xi}}C_2\right)\sqrt{1+\frac{1}{\xi}}\sin\left[\frac{L_1\log(k+r)}{\sqrt{1+\frac{1}{\xi}}}\right]\right]\right\}$$

$$\theta\left(x,r\right)=B_2-\frac{\mathrm{Br}}{4+\mathrm{Pr}\,R_d}\cdot$$

$$\cdot\left(\frac{-\left[k^2\frac{\mathrm{d}p}{\mathrm{d}x}^2r(k+r)\right]}{\mathrm{M}^2}-\frac{1}{\mathrm{M}^4}\left\{8k\frac{\mathrm{d}p}{\mathrm{d}x}(k+r)\left(-2L_1\sqrt{1+\frac{1}{\xi}}C_2+L_3C_1\right)\cos\left[\frac{L_1\log(k+r)}{\sqrt{1+\frac{1}{\xi}}}\right]\right]\right\}\right)+$$

$$+\frac{1}{L_1}\left(-L_1C_1^2+L_1C_2^2-2C_1C_2\sqrt{1+\frac{1}{\xi}}\right)\sqrt{1+\frac{1}{\xi}}\cos\left[\frac{2L_1\log(k+r)}{\sqrt{1+\frac{1}{\xi}}}\right]+$$

$$+\frac{2\log(k+r)}{\mathrm{Br}\,\mathrm{M}^2}\left[\mathrm{Br}\,k^2\frac{\mathrm{d}p}{\mathrm{d}x}^2+2M^2\left(1+\mathrm{Pr}\,R_d\right)B_1\right]+$$

$$+\frac{1}{\mathrm{M}^4}\left\{8k\frac{\mathrm{d}p}{\mathrm{d}x}(k+r)\left(2L_1\sqrt{1+\frac{1}{\xi}}C_1+L_3C_2\right)\sqrt{1+\frac{1}{\xi}}\sin\left[\frac{L_1\log(k+r)}{\sqrt{1+\frac{1}{\xi}}}\right]\right\}+$$

$$+\frac{1}{L_1}\left(C_1^2\sqrt{1+\frac{1}{\xi}}-C_2^2\sqrt{1+\frac{1}{\xi}}-2C_1C_2L_1\right)\sqrt{1+\frac{1}{\xi}}\sin\left[\frac{L_1\log(k+r)}{\sqrt{1+\frac{1}{\xi}}}\right]\Bigg\}$$

$$\frac{\mathrm{d}p}{\mathrm{d}x}=-\frac{\mathrm{M}^2\left(F+2\eta\right)\sin\left(L_2\right)}{2k\left[\begin{array}{c}L_1\sqrt{1+\frac{1}{\xi}}\left(-k^2+\eta^2\right)+L_1\sqrt{1+\frac{1}{\xi}}\left(k^2+\eta^2\right)\cos\left(L_2\right)+\\+k\eta\left[\mathrm{M}^2+2\left(1+\frac{1}{\xi}\right)\sin\left(L_2\right)\right]\end{array}\right]}$$

where

$$L_1=\sqrt{-M^2-\left(1+\frac{1}{\xi}\right)},\quad L_2=\frac{L_1\left[\log\left(k-\eta\right)-\log\left(k-\eta\right)\right]}{\left(1+\frac{1}{\xi}\right)}$$

Discussion

Pumping phenomena

The purpose of this section is to explain impacts of different physical parameters. Responses of the pressure gradient for different values of amplitude ratio, ϵ, Hartmann number, M, curvature parameter, k, and Casson fluid parameter, ξ, are shown in the figs. 2-5, respectively. It is observed that pressure gradient $\mathrm{d}p/\mathrm{d}x$ rises upward when the amplitude ratio ϵ and Hartmann number are increased, see figs. 2 and 3. It means that for larger amplitude ratio ϵ the clasping and compressing phenomena are affected. Radially imposed magnetic field play an important role for the pressure gradient $\mathrm{d}p/\mathrm{d}x$ against the resistive forces of the flow. Figures 4 and 5 illustrate that the pressure gradient $\mathrm{d}p/\mathrm{d}x$ decreases when curvature parameter, k, and Casson fluid parameter, ξ, are enhanced. It is important to note that the pressure gradient is greater for Casson fluid when compared with viscous fluid. The pressure rises per wavelength Δp_λ is the quantity which shows the flow behavior for different pumping regions. It is very difficult to evaluate pressure rise per wavelength Δp_λ analytically. Hence numerical integration is used to compute its expression. It is very important to know that the pressure rise per wave-

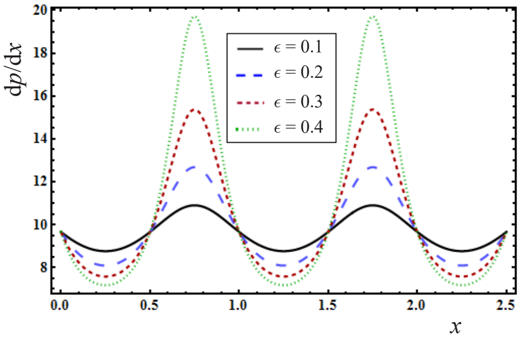

Figure 2. Shows d*p*/d*x* for ϵ with $\xi = 10^3$, $\Theta = 1$, M = 2, $k = 3$

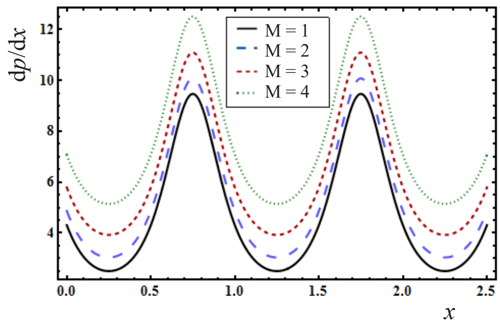

Figure 3. Shows d*p*/d*x* for M with $\xi = 10^3$, $\Theta = 1$, $\epsilon = 0.3$, $k = 3$

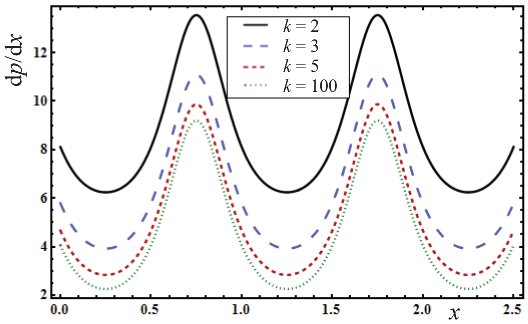

Figure 4. Shows d*p*/d*x* for k with $\xi = 10^3$, $\Theta = 1$, $\epsilon = 0.3$, M = 2

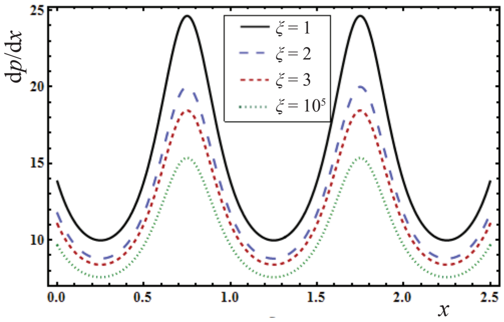

Figure 5: Shows d*p*/d*x* for ξ with $k = 3$, $\Theta = 1$, $\epsilon = 0.3$, M = 2

length studies the fluid-flow in three different regions *i. e.* peristaltic pumping region ($\Delta p_\lambda > 0$), free pumping region ($\Delta p_\lambda = 0$) and copumping region ($\Delta p_\lambda < 0$). Figure 6 shows that the pressure rise per wavelength increases peristaltic ($\Delta p_\lambda > 0$) and free pumping ($\Delta p_\lambda = 0$) regions whereas it decreases in copumping region ($\Delta p_\lambda < 0$) as we increase the amplitude ratio ϵ . Pressure rise per wavelength Δp_λ increases in the peristaltic pumping region ($\Delta p_\lambda > 0$) and it decreases in the copumping region ($\Delta p_\lambda < 0$) through Hartmann number, see fig. 7. Opposite behavior of pressure rise per wavelength Δp_λ is observed for different values of curvature parameter, k, and Casson fluid parameter, ξ, see figs. 8 and 9. From figs. 7 and 8 it is very easy

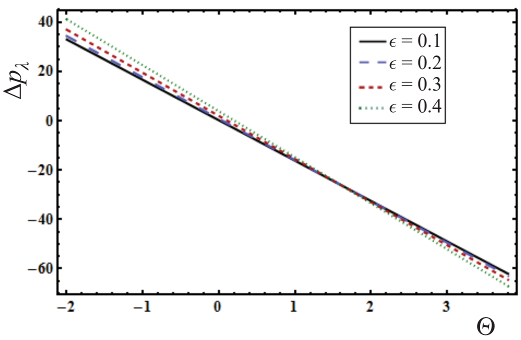

Figure 6. Shows Δp_λ for ϵ with $\xi = 10^3$, M = 2, $k = 3$

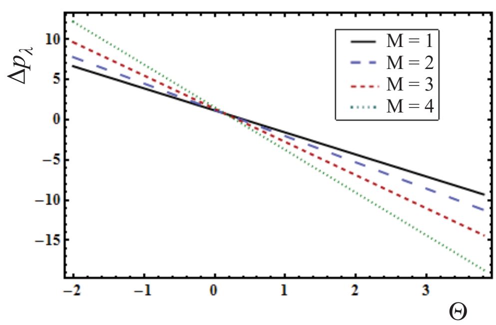

Figure 7: Shows Δp_λ for M with $\xi = 10^3$, $\epsilon = 0.3$, $k = 3$

to observe that the peristaltic phenomenon is present. It is found that the pressure rises per wavelength Δp_λ is low for viscous fluid when compared with Casson fluid.

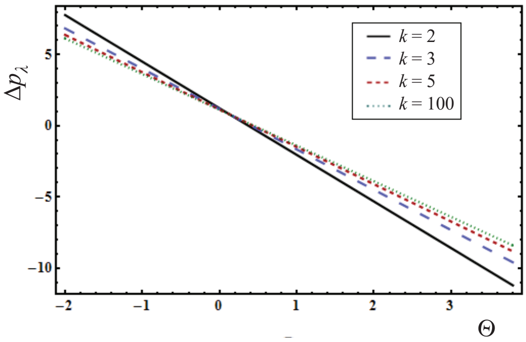

Figure 8. Shows Δp_λ for k with $\xi = 10^3$, $\epsilon = 0.3$, M = 2

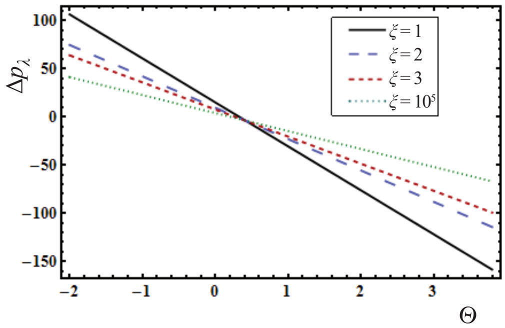

Figure 9. Shows Δp_λ for ξ with M = 2, $\epsilon = 0.3$, $k = 3$

Velocity

Variations of different parameters of interest on the velocity are displayed in the figs. 10-17. Here 3-D plots are presented. Figure 10 shows that velocity near lower wall decreases while it increases near upper wall when curvature parameter, k, is increased. Figure 11 depicts that velocity decreases at the centre of the channel and it enhances near the walls of curved channel when Hartmann number is increased. Figure 12 has the similar qualitative effect for Casson fluid as that of Hartmann number on the velocity in fig. 11. Further magnitude of velocity in Casson fluid is more than that of viscous fluid. The 3-D plot captured in fig. 14 show that velocity is increasing function of volume flow rate, Θ.

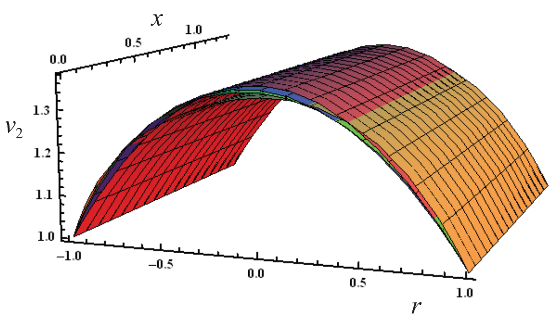

Figure 10. Shows v_2 for k with $\xi = 10^3$, $\Theta = 1$, $\epsilon = 0.3$, M = 2, $x = 0$

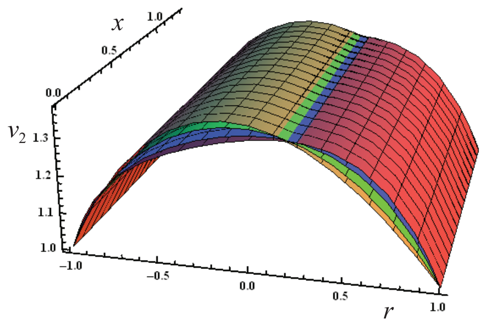

Figure 11. Shows v_2 for M with $\xi = 10^3$, $\Theta = 1$, $\epsilon = 0.3$, $k = 3$, $x = 0$

Temperature

Figures 14-18 are prepared to describe the impact of embedded parameters of interest on temperature through 3-D plots. Figure 14 discloses, the behavior of temperature for curvature, k. This figure indicates that temperature decays at centre and it rises near the channel walls. Evidently, temperature rises due to slow velocity field for larger Hartmann number, see fig. 15. Physical, Lorentz force is responsible for this because it resist the flow field as a result fluid particles dissipates energy thus temperature rises. Similar situation is observed in fig. 16

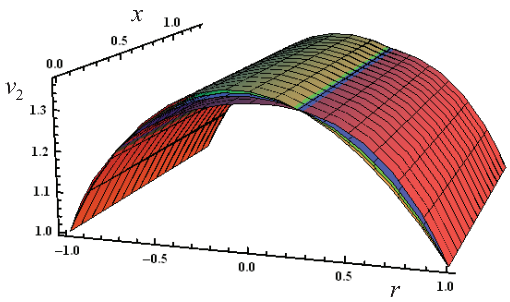

Figure 12. Shows v_2 for ξ with k = 3, Θ = 1, ϵ = 0.3, M = 2, x = 0

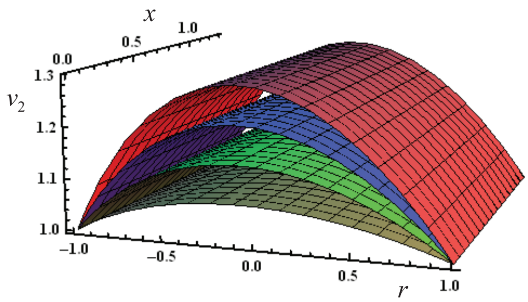

Figure 13. Shows v_2 for Θ with k = 3, $\xi = 10^3$, ϵ = 0.3, M = 2, x = 0

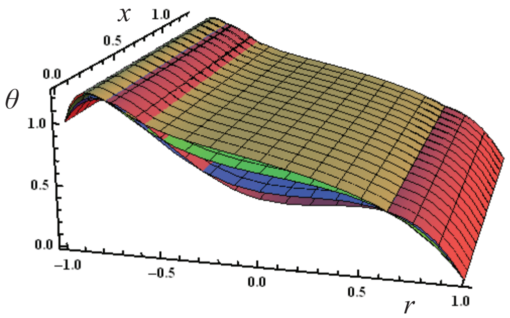

Figure 14. Shows θ for k with $\xi = 10^3$, Θ = 1, ϵ = 0.3, M = 2, x = 0, Pr = 2, Br = 2, R_d = 0.5

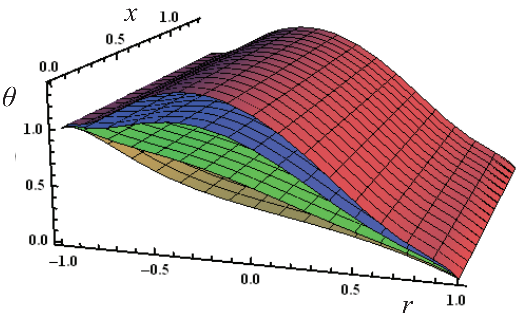

Figure 15. Shows θ for M with $\xi = 10^3$, Θ = 1, ϵ = 0.3, k = 3, x = 0, Pr = 2, Br = 2, R_d = 0.5

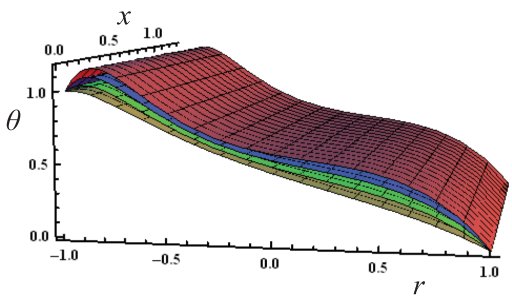

Figure 16. Shows θ for Br with $\xi = 10^3$, Θ = 1, ϵ = 0.3, M = 2, x = 0, Pr = 2, k = 3, R_d = 0.5

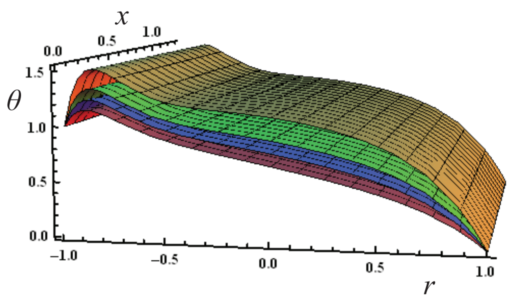

Figure 17. Shows θ for R_d with $\xi = 10^3$, Θ = 1, ϵ = 0.3, M = 2, x = 0, Pr = 2, k = 3, Br = 2

temperature for Brinkman number as for Hartmann number shown in fig. 15. Figure 17 corresponds to the behavior of temperature for different values of thermal radiation parameter, R_d. This figure indicates the temperature reduces significantly with the enhancement of R_d. Similarly, temperature also reduces for Prandtl number, see fig. 18.

Note that the parameter values used in 3-D plots versus different colours are disclosed in tab. 1.

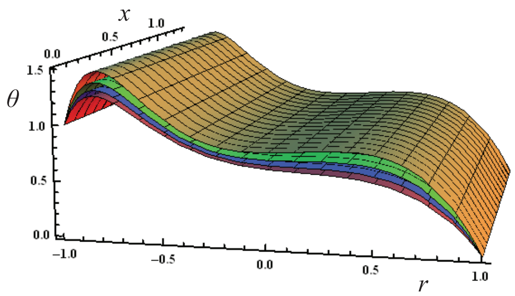

Figure 18. Shows θ for Pr with $\xi = 10^3$, $\Theta = 1$, $\epsilon = 0.3$, M = 2, $x = 0$, Br = 2, $k = 3$, $R_d = 0.5$

Table 1. Parameter values for each 3-D curves made for velocity and temperature

Parameters	Colour name for 3-D curve			
	Orange	Green	Blue	Red
k	2	3	4	100
M	1	2	3	4
ξ	1	3	5	
Θ	0.1	0.2	0.3	0.4
Br	0.5	1.0	1.5	2.0
R_d	0.0	0.4	0.8	1.5
Pr	0.5	1.0	1.5	2.0

Streamlines

Now the figs. 19-22 have been prepared for the outcome of different embedding parameters on the trapped bolus. Figure 19 depicts that shape of trapped bolus is increasing function of amplitude ratio parameter, ϵ. Effect of curvature parameter, k, on trapping bolus is plotted in fig. 20. Here trapped bolus decreases for increasing values of curvature parameter, k. It is noted that for $k = 100$ the trapped bolus splits away. Figure 21 depicts that the trapped bolus decreases in size for larger values of Hartmann number. For Casson fluid model the trapped bolus decreases, see fig. 22. It is very interesting to know that the size of trapped bolus in Casson fluid is larger than for Newtonian fluid.

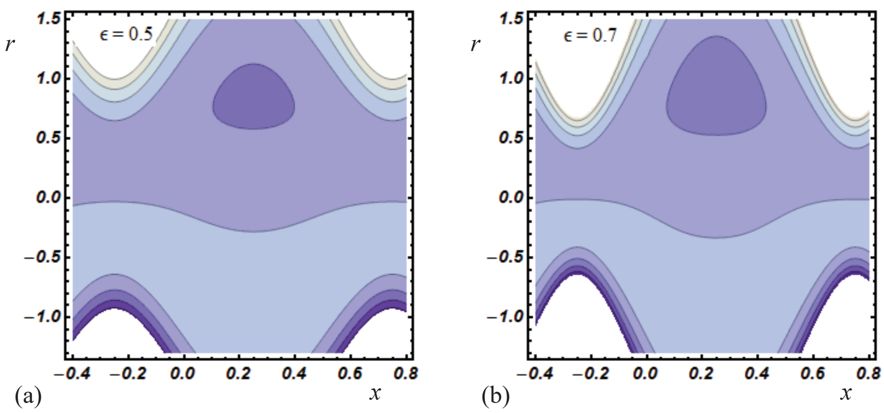

Figure 19. Streamlines for ϵ with $k = 3$, M = 5.5, $\xi = 10^3$, $\Theta = 2.7$

Concluding remarks

The main observations are given as follows.

- Symmetry of velocity profile is disturbed at centre line in curved channel situation.
- Velocity for Casson fluid is more than the viscous material.
- Temperature has similar response for thermal radiation and Prandtl number.
- Temperature enhances for both Hartmann and Brinkman numbers due to higher amount of collision between fluid particles.
- Behaviors of Hartmann number, curvature and Casson fluid parameter on the trapped bolus are qualitatively similar.
- Variations of Hartmann number and amplitude ratio on the trapped bolus are opposite.

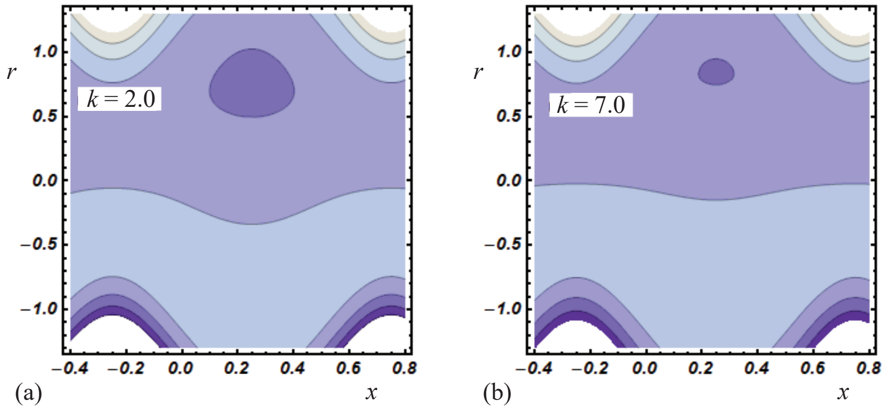

Figure 20. Streamlines for k with ϵ = 0,4, M = 5.5, $\xi = 10^3$, Θ = 2.7

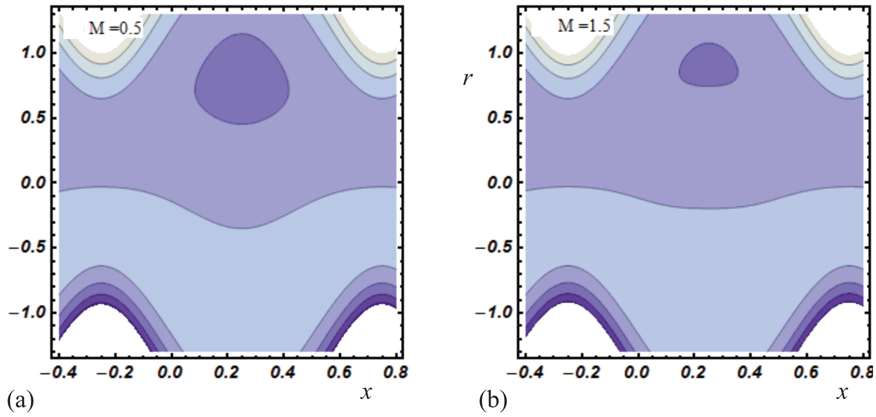

Figure 21. Streamlines for M with ϵ = 0,4, k = 3, $\xi = 10^3$, Θ = 2.7

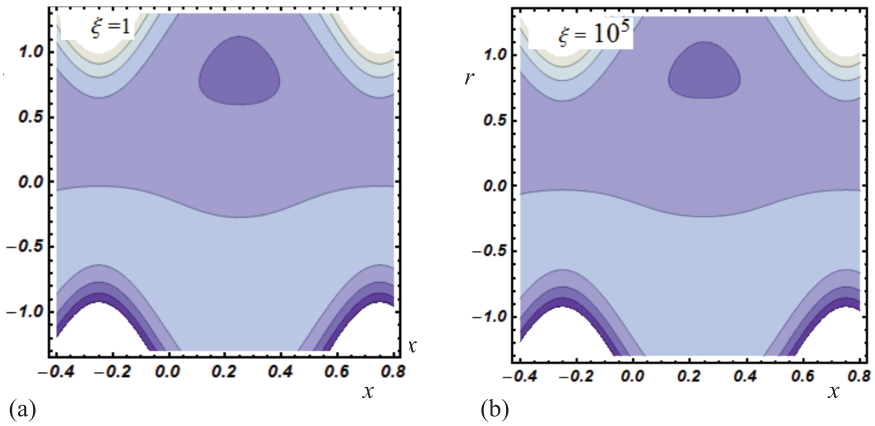

Figure 22. Streamlines for ξ with ϵ = 0,4, k = 3, M = 5.5, Θ = 2.7

References

[1] Latham, T. W., *Fluid Motion in a Peristaltic Pump*, MIT, Cambridge, Mass, USA 1966
[2] Shapiro, A. H., *et al.*, Peristaltic Pumping with Long Wavelength at Low Reynolds Number, *J. Fluid Mech.*, *37* (1969), July, pp. 799-825

[3] Mekheimer, Kh. S., *et al.*, Particulate Suspension Flow Induced by Sinusoidal Peristaltic Waves through Eccentric Cylinders: Thread Annular, *Int. J. Biomath., 06* (2013), 04, 1350026
[4] Tripathi, D., A Mathematical Model for Swallowing of Food Bolus Through the Esophagus under the Influence of Heat Transfer, *Int. J. Therm. Sci., 51* (2012), Jan., pp. 91-101
[5] Mekheimer, Kh. S., Abd Elmaboud, Y., Simultaneous Effects of Variable Viscosity and Thermal Conductivity on Peristaltic Flow in a Vertical Asymmetric Channel, *Can. J. Phys., 92* (2014), 12, pp. 1541-1555
[6] Sinha, A., *et al.*, Peristaltic Transport of MHD Flow and Heat Transfer in an Asymmetric Channel: Effects of Variable Viscosity, Velocity-Slip and Temperature Jump, *Alexandria Eng. J., 54* (2015), 3, pp. 691-704
[7] Awais, M., *et al.*, Convective Heat Transfer Analysis for MHD Peristaltic Flow of Jeffrey Fluid in an Asymmetric Channel, *Int. J. Biomath., 07* (2014), 03, 1450023
[8] Ellahi, R., *et al.*, The Effect of Magnetohydrodynamics on Peristaltic Flow of Jeffrey Fluid in a Rectangular Duct Through a Porous Medium, *J. Porous Media, 17* (2014), 2, pp. 143-157
[9] Asghar, S., *et al.*, Existence of a Hartmann Layer in the Peristalsis of Sisko Fluid, *Chin. Phys. B, 23* (2014), 5, pp. 054702-054707.
[10] Khan, A. A., *et al.*, Effects of Heat Transfer on Peristaltic Motion of Oldroyd Fluid in the Presence of Inclined Magnetic Field, *J. Magn. Magn. Mater., 372* (2014), Dec., pp. 97-106
[11] Kothandapani, M., Srinivas, S., Peristaltic Transport of Jeffrey Fluid under the Effect of Magnetic Field in an Asymmetric Channel, *Int. J. Non-Linear Mech., 43* (2012), 9, pp. 915-924
[12] Mekheimer, Kh. S., *et al.*, Simultaneous Effects of Magnetic Field and Space Porosity on Compressible Maxwell Fluid Transport Induced by a Surface Acoustic Wave in a Microchannel, *Chin. Phys. B., 22* (2013), 12, 124702
[13] Sato, H., *et al.*, Two Dimensional Peristaltic Flow in Curved Channels, *Trans. Jpn. Soc. Mech. Eng., B 66* (2000), 643, pp. 679-685
[14] Ali, N., *et al.*, An Analysis of Peristaltic Flow of Micropolar Fluid in a Curved Channel, *Chin. Phy. Lett., 28* (2011), 1, 014704
[15] Ali, N., *et al.*, Long Wavelength Flow Analysis on Curved Channel, *Z. Naturforsch. A, 65* (2010), 3, pp. 191-196
[16] Hina, S., *et al.*, On Peristaltic Motion of Pseudoplastic Fluid in a Curved Channel with Heat/Mass Transfer and Wall Properties, *Appl. Math. Comput., 263* (2015), July, pp. 378-391
[17] Shehzad, S. A., *et al.*, Peristalsis in a Curved Channel with Slip Condition and Radial Magnetic Field, *Int. J. Heat Mass Transfer, 91* (2015), Dec., pp. 562-569
[18] Hayat, T., *et al.*, Peristaltic Transport of Viscous Fluid in a Curved Channel with Compliant Walls, *54* (2011), 7-8, pp. 1615-1621
[19] Ali, N., *et al.*, Non-Newtonian Fluid Flow Induced by Peristaltic Waves in a Curved Channel, *Eur. J. Mech. B/Fluids, 29* (2010), 5, pp. 387-394
[20] Hayat, T., *et al.*, Homogeneous-Heterogeneous Reactions Effects in Peristalsis through Curved Geometry, *AIP Advances, 5* (2015), 6, 067172
[21] Pal, D., Mandal, G., Hydromagnetic Convective-Radiative Boundary Layer Flow of Nanofluids Induced by a Non-Linear Vertical Stretching/Shrinking Sheet with Viscous-Ohmic Dissipation, *Powder Technol., 279* (2015), July, pp. 61-74
[22] Sheikholeslami, M., *et al.*, MHD Free Convection of Al_2O_3-Water Nanofluid Considering Thermal Radiation: A Numerical Study, *Int. J. Heat Mass Transf., 96* (2016), May, pp. 513-524
[23] Hayat, T., *et al.*, Effectiveness of Magnetic Nanoparticles in Radiative Flow of Eyring-Powell Fluid, *J. Mol. Liq., 231* (2017), Apr., pp. 126-133
[24] Hayat, T., *et al.*, Simultaneous Effects of Heat Generation/Absorption and Thermal Radiation in Magnetohydrodynamics (MHD) Flow of Maxwell Nanofluid Towards a Stretched Surface, *Results Phys., 7* (2017), Jan., pp. 562-573
[25] Bhatti, M. M., Rashidi, M. M., Effects of Thermo-Diffusion and Thermal Radiation on Williamson Nanofluid over a Porous Shrinking/Stretching Sheet, *J. Mol. Liq., 221* (2016), Sept., pp. 567-573
[26] Hayat, T., *et al.*, Hall and Radial Magnetic Field Effects on Radiative Peristaltic Flow of Carreau-Yasuda Fluid in a Channel with Convective Heat and Mass Transfer, *J. Mag. Mag. Mat. 412* (2016), Aug., pp. 207-216
[27] Farooq, S., *et al.*, Mixed Convection Peristalsis of Carbon Nanotubes with Thermal Radiation and Entropy Generation, *J. Mol. Liq. 250* (2018), Jan., pp. 451-467
[28] Hayat, T., *et al.*, Peristalsis of Eyring-Powell Magneto Nanomaterial Considering Darcy-Forchheimer Relation, *Int. J. Heat Mass Transf. 115* (2017), Part A, pp. 694-702

[29] Prakash, J., Tripathi, D., Electroosmotic Flow of Williamson Ionic Nanoliquids in a Tapered Microfluidic Channel in Presence of Thermal Radiation and Peristalsis, *J. Mol. Liq. 256* (2018), Apr., pp. 352-371
[30] Prakash, J., *et al.*, Thermal Radiation Effects on Electroosmosis Modulated Peristaltic Transport of Ionic Nanoliquids in Biomicrofluidics Channel, *J. Mol. Liq. 249* (2018), Jan., pp. 843-855
[31] Casson, N., *Rheology of Disperse Systems*, Pergamon Press, Oxford, UK, 1959
[32] Herschel, W. H., Bulkley, R., Measurement of Consistency as Applied to Rubber-Benzene Solutions, *Am. Soc. Test. Proc. 26* (1926), p. 621
[33] Bingham, E., The Behavior of Plastic Materials, *Bull. US. Bur. Stand. 13* (1916), pp. 309-353
[34] Steffe, J. F., *Rheological Methods in Food Process Engineering*, Freeman Press, Gambrilla, Md., USA, 1996
[35] Hussain, T., *et al.*, Impact of Magnetic Field in Radiative Flow of Casson Nanofluid with Heat and Mass Fluxes, *Thermal Science, 22* (2018), 1A, pp. 137-145
[36] Hayat, T., *et al.*, Soret and Dufour Effects on Magnetohydrodynamic (MHD) Flow of Casson Fluid, *Appl. Math. Mech. 33* (2012), 10, pp. 1301-1312
[37] Benazir, A. J., *et al.*, Unsteady Magnetohydrodynamic Casson Fluid Flow over a Vertical Cone and Flat Plate with Non-Uniform Heat Source/Sink, *Int. J. Eng. Res. Africa. 21* (2015), Dec., pp. 69-83
[38] Rehman, K. U., *et al.*, Numerical Study of Double Stratification in Casson Fluid Flow in the Presence of Mixed Convection and Chemical Reaction, *Results Phys., 7* (2017), pp. 2997-3006
[39] Chakravarty, S., *et al.*, Unsteady Flow of a Two-Layer Blood Stream Past a Tapered Flexible Artery under Stenotic Conditions, *Comput. Methods Appl. Math. 4* (2004), 4, pp. 391-409
[40] Iida, N., Influence of Plasma Layer on Steady Blood Flow in Microvessels, *Jpn. J. Appl. Phys. 17* (1978), 1, pp. 203-214
[41] Aghighi, M. S., *et al.*, Rayleigh-Bénard Cconvection of Casson Fluids, *Int. J. Thermal Sci. 127* (2018), May, pp. 79-90
[42] Mahanthesh, B., Gireesha, B. J., Thermal Marangoni Convection in Two-Phase Flow of Dusty Casson Fluid, *Results Phy. 8* (2018), Mar., pp. 537-544
[43] Khan, M. I., *et al.*, A Comparative Study of Casson Fluid with Homogeneous-Heterogeneous Reactions, *J. Colloid Interface Sci., 498* (2017), July, pp. 85-90
[44] Malik, M. Y., *et al.*, Variable Viscosity and MHD Flow in Casson Fluid with Cattaneo-Christov Heat Flux Model: Using Keller Box Method, *Eng. Sci. Tech. Int. J., 19* (2016), 4, pp. 1985-1992
[45] Tamoor, M., *et al.*, Magnetohydrodynamic Flow of Casson Fluid over a Stretching Cylinder, *Results Phy., 7* (2017), Jan., pp. 498-502
[46] Srivastava, L. M., Srivastava, V. P., Peristaltic Transport of a Power Law Fluid: Applications to the Ductus Efferentes of the Reproductive Tract, *Rheologica Acta., 27* (1988), 4, pp. 428-433
[47] Lew, H. S., *et al.*, Peristaltic Carrying and Mixing of Chyme in the Small Intestine, *J. Biomech., 4* (1971), 4, pp. 297-315
[48] Hayat, T., *et al.*, Homogeneous-Heterogeneous Reactions and Heat Source/Sink Effects in MHD Peristaltic Flow of Micropolar Fluid with Newtonian Heating in a Curved Channel, *J. Mol. Liq., 223* (2016), Nov., pp. 469-488
[49] Hayat, T., *et al.*, Numerical Study for Soret and Dufour Effects on Mixed Convective Peristalsis of Oldroyd 8-Constants Fluid, *Int. J. Thermal Sci., 112* (2017), Feb., pp. 68-81
[50] Hayat, T., *et al.*, Simultaneous Effects of Hall Current and Homogeneous/Heterogeneous Reactions on Peristalsis, *J. Taiwan Inst. Chem. Eng., 58* (2016), Jan., pp. 28-38

Paper submitted: January 4, 2018
Paper revised: April 6, 2018
Paper accepted: April 9, 2018